This is the accepted manuscript version of the contribution published as:

Liu, Y.-J., Yang, H.-Y., **Gao, S.-X.**, Li, Z.-H., Hu, Y.-Y., Zheng, X., Sheng, G.-P. (2025): Molecular fractionation mediates genotoxicity evolution of hydrochar-derived dissolved organic matter at the iron oxyhydroxides-water interface
Water Res. **268, Part A** , art. 122584

The publisher's version is available at:

https://doi.org/10.1016/j.watres.2024.122584

Revised manuscript (clean version)

Click here to view linked References

Molecular fractionation mediates genotoxicity evolution of hydrochar-derived dissolved organic matter at the iron oxyhydroxides-water interface

Yan-Jun Liu[a#], He-Yun Yang[b#], Shu-Xian Gao[c], Zheng-Hao Li[a*], Yan-Yun Hu[d], Xing Zheng[b], and Guo-Ping Sheng[a*]

[a]CAS Key Laboratory of Urban Pollutant Conversion, Department of Environmental Science and Engineering, University of Science and Technology of China, Hefei, 230026, China

[b]State Key Laboratory of Eco-hydraulics in Northwest Arid Region, Xi'an University of Technology, Xi'an, 710048, China

[c]Research Group BioGeoOmics, Department Environmental Analytical Chemistry, Helmholtz Centre for Environmental Research - UFZ, Permoserstr. 15, Leipzig D-04318, Germany

[d]Instruments Center for Physical Science, University of Science and Technology of China, Hefei, 230026, China

***Corresponding Authors:**

Zheng-Hao Li: E-mail: lizhhao@ustc.edu.cn

Guo-Ping Sheng: E-mail: gpsheng@ustc.edu.cn

[#]Yan-Jun Liu and He-Yun Yang contributed equally to this paper

Abstract

Adsorption fractionation of dissolved organic matter (DOM) induced by soil minerals is a common geochemical process, which has been widely documented on natural DOM. Hydrochar is a promising functional material in soil remediation but can continuously release abundant endogenic DOM with potential biotoxicity. However, adsorption fractionation at molecular level and its influence on toxicity evolution of hydrochar-derived DOM (HDOM) at genetic level at the soil-water interface remain poorly understood. Herein, we investigated the molecular fractionation of HDOM on three typical soil iron minerals (i.e., ferrihydrite, goethite, and hematite). Results from ultrahigh-resolution mass spectrum showed that HDOM molecules with high molecular weight and high contents of unsaturated oxidized or aromatic structures (e.g., unsaturated phenolic compounds, polyphenols, and organic acids) were preferentially absorbed by iron oxyhydroxides, while aliphatic molecules and poorly oxygenated compounds (e.g., hydrocarbon, phenols, and alcohols) were retained in aqueous phase. Furthermore, we quantitatively evaluated their genotoxicity variation using a toxicogenomics assay using green fluorescence protein-fused whole-cell array, and results showed that oxidative, protein, membrane, and DNA stress was primary responses upon exposure to original HDOM. Interface fractionation induced by iron oxyhydroxides significantly reduced genotoxicity of HDOM, especially for oxidative, membrane and DNA stresses. Overall, the selective absorption of HDOM molecules by iron oxyhydroxides shifted its biotoxicity, which might change the ecological effects of hydrochar amendment, e.g., microbial community structure, environmental pollutant transformation, and even the ecological function of terrestrial and aquatic ecosystems. These findings would contribute to unravel the environmental geochemistry process of HDOM in the natural soil-water interface and provide a new insight into the biotoxicity of hydrochar usage to terrestrial and aquatic environments.

Keywords: Hydrochar; Dissolved organic matter; Molecular fractionation; Toxicogenomics assay; Soil-water interface

1. Introduction

Application of biochar into agricultural soils is considered as a promising strategy for carbon sequestration and greenhouse gas mitigation in the context of global carbon emissions reduction (Xia et al., 2023). The global biochar market was valued at USD 1.5 billion in 2022 and is expected to reach USD 4.2 billion by 2030, which means that over 135,000 tons of biochar are used in agricultural fields annually (Zhang et al., 2019). Hydrochar is an emerging type of biochar synthesized at 180-340 ℃ in a closed system with saturated vapor pressure (Magdziarz et al., 2020). Compared to pyrochar produced by conventional dry pyrolysis, hydrochar produced from hydrothermal liquefaction has received more attention due to the cost-effectively direct transformation of wet biomass without pre-drying and simultaneously higher yields of products (Yan et al., 2010). Currently, hydrochar has been widely used as soil amendments because they can immobilize contaminants (e.g., heavy metals and organic chemicals), increase soil fertility, and hasten crop growth due to their strong adsorption capacity, excellent hole structure, and high nutrient content (Luo et al., 2023; Xiang et al., 2022). Nevertheless, the potential ecological risks of hydrochar application in soil amendment has been neglected for quite a long time. The prepared hydrochar exhibits less stable structure and high oxygen-containing functional groups due to the low temperature of hydrothermal carbonization (Sun et al., 2020). Additionally, hydrochar can persist for a long time in the soil due to it is carbon-based material, which might undergo various aging effects including microbial, sunlight, and precipitation during this process (Ge et al., 2024). As a result, the abundant endogenic dissolved organic matter can be readily released from hydrochar after being applied in soil system, and potentially infiltrating into the groundwater layer or transporting to surface water along with precipitation and surface runoff. However, unlike natural organic matter, hydrochar-derived dissolved organic matter (HDOM) contained a higher

content of phenols, polyphenols, and organic acids which have been reported to have potential biotoxicity to aquatic biota (Ennis et al., 2012; Hao et al., 2018). Therefore, it is crucial to gain a comprehensive understanding of the environmental processes and ecological impacts of HDOM to terrestrial and aquatic environments in the soil-water interface when using hydrochar for practical soil remediation.

Soil minerals serve as vital barriers against the migration of pollutants (e.g., percolation into groundwater or transport to surface water), which greatly influence the distribution and potential environmental risks of pollutants at soil-water interface due to their diverse adsorption capacities. Among various soil minerals, iron oxyhydroxides play an important role in controlling the fate and transport of organic compounds due to their wide distribution, large specific surface area, and abundant hydroxyl sites (Lalonde et al., 2012; Melton et al., 2014; Ye et al., 2023; Zhao et al., 2022). For instance, previous study reported that the loading of goethite increased the sorption affinity of pyrene to quartz the through non-covalent cation-π interaction, and prevented their further migration into groundwater (Mueller et al., 2007). Hanna et al (2007) also revealed that the transport of aromatic carboxylate compounds (e.g., gentisic acid and 1-hydroxy-2-naphthoic acid) in the soil could be strongly intercepted by iron oxyhydroxides. In addition, a recent study demonstrated that the addition of natural hematite enhanced the removal (closed to 99% after 7 days) of phenol pollutants through increasing soil porosity (Zhang et al., 2023). As a vital potential source of aromatic organics, the interaction between HDOM molecules with iron oxyhydroxides and its influence on evolution of potential ecotoxicity are necessary to be studied, which was not investigated in-depth by previous studies. For instance, prior studies investigated the interactions between various DOM and iron minerals via chromatography and spectroscopic methods, and found that high molecular weight, hydrophobic, aromatic, and carboxylic fractions are

preferentially retained on iron mineral surfaces (Ennis et al., 2012; Huang et al., 2018). In addition, a recent study reported that HDOM significantly caused inhibition cyanobacterial growth, and its biotoxicity increased with the elevation of production temperature (180-330 ℃) (Hao et al., 2018). However, the detailed adsorption process at molecular level and its influence on toxicity evolution of HDOM at genetic level during the fractionation process on iron oxyhydroxides remain so far largely unknown, which greatly limited the in-depth understanding the potential ecological risk of hydrochar application in soil amendment.

Recently, the remarkable development of high-resolution mass spectrum techniques makes it possible to analysis DOM at molecular level. Fourier transform-ion cyclotron resonance mass spectrometry (FT-ICR MS) is a non-targeted mass spectrometry with ultrahigh resolution and low detection limits, which has been proved to reveal the molecular composition of complex organic chemicals from aquatic and terrestrial environments (Fu et al., 2020a), which may provide novel insights into the chemical nature of organic matters based on their accurate molecular formulas (Feng and Siegel, 2007; Gao et al., 2021). With the help of this technique, thousands of molecular formulas in HDOM can be obtained unambiguously, which contributing to elucidate the molecular composition variation of HDOM during the adsorption process on iron oxyhydroxides with more precision. In addition, a toxicogenomics-based toxicity assessment approach could monitor thousands of genes corresponded to external stressors in transcription and expression levels with one single assay within 2 - 4 h, and provide comprehensive information to demonstrate the pollutant-specific toxicity profiles and molecular mechanisms (Gou et al., 2010; Gou et al., 2011). This method has been successfully applied to screen various contaminants, such as nanomaterials, heavy metals, and organic pollutants, to evaluate their genotoxicity and potential environmental

risks (Gou et al., 2011; Gou et al., 2010; Gou et al., 2014; Liu et al., 2023; Zheng et al., 2020). Therefore, the utilization of this platform can offer pollutant-specific toxicity mechanisms, which may deepen our understanding on genotoxicity evolution of HDOM before and after adsorption by iron oxyhydroxides. Hence, we suppose that these high-resolution, high-sensitive, and high-throughput techniques are feasible to clarify the distribution and environmental risks of HDOM in soil-water ecosystems.

Therefore, the objectives of this study were to comprehensively investigate the fate and transport of HDOM in soil-water interface and reveal genotoxicity evolution of HDOM during adsorption fractionation at molecular level. Three types of typical iron oxyhydroxides (i.e., ferrihydrite, goethite, and hematite) were selected in the present study since they are vital mineral components in soil-water environments and play an important role in adsorption of organic matter (Wu et al., 2023). All experiments were conducted in iron oxyhydroxides suspension system to exclude the disturb of environmental factors and obtain accurate mechanisms at molecular level. Fourier Transform Infrared Spectroscopy (FTIR), and X-ray photoelectron spectroscopy (XPS), and FT-ICR MS were conducted to elucidate the interaction mechanisms of between iron oxyhydroxides and HDOM. Subsequently, a quantitative toxicogenomics-based assay was employed to reveal their genotoxicity and intrinsic mechanisms before and after sorption by iron oxyhydroxides at the molecular level. Lastly, correlation analysis between the FT-ICR-MS molecular parameters and genotoxicity was conducted to further demonstrate the effects of molecular fractionation on genotoxicity evolution of HDOM. Overall, our results would be helpful to understand the geochemical behaviors and ecological risks of hydrochar-derived dissolved organic matter in soil-water systems, providing a guideline for hydrochar application on a large scale in the future.

2. Material and methods

2.1. Preparation and characterization of iron oxyhydroxides and hydrochar

The iron oxyhydroxides including ferrihydrite and goethite were synthesized according to methods reported by previous studies (details were given in the Supporting Information) (Ona-Nguema et al., 2005; Wang et al., 2021), while hematite was purchased from Sigma-Aldrich (US). All iron oxyhydroxides were repeatedly washed with ultrapure water (> 18.2 MΩ·cm) and freeze-dried before experiments and characterizations. X-ray diffraction (XRD) and scanning electron microscope (SEM) analysis indicate that the obtained iron oxyhydroxides were standard 2-line ferrihydrite, goethite and hematite, respectively (Fig. S1). The Brunauer-Emmett-Teller specific surface areas (SSA) and pore size of each iron oxyhydroxides were examined by N_2 adsorption−desorption (Tristar II 3020M, Micromeritics, US). The zeta potentials of ferrihydrite, goethite and hematite were characterized using a Zetasizer Nano ZS (Malvern Instruments, UK).

Hydrochar was produced from rice straw powder through hydrothermal carbonization at 200°C for 2 h (detailed preparation procedures and characterization were provided in the Supporting Information) according to previous studies (Hao et al., 2018; Zhang et al., 2020). The HDOM extraction was conducted following the similar procedures reported by previous studies (Lv et al., 2016; Zhang et al., 2020). The release of HDOM from hydrochar was performed by shaking 0.3 g sample in 100 mL ultrapure water for 24 h (200 rpm, 25 ℃). The HDOM was collected by centrifugation at 6000 rpm for 10 min and then filtering through a 0.45 μm mixed cellulose ester membrane. The obtained HDOM solution was kept in the dark at 4 ℃ and used within 7 days after extraction. The total organic carbon (TOC) concentration of HDOM was

142 determined using a TOC analyzer (Vario, Elementar, Germany). UV-vis spectrum of HDOM was
143 collected (UV-2600, Shimadzu, Japan), and the corresponding $SUVA_{254}$ values were calculated.
144 Additionally, to avoid polymer pollution, all vessels used in this work are glassware and combusted
145 at 450 ℃ for 2 h before used.
146
147 *2.2. Batch adsorption experiments*
148 To simulate the interaction between HDOM and iron oxyhydroxides, batch adsorption
149 experiments of HDOM (10-100 mg-C/L) onto iron oxyhydroxide suspensions (1 g/L ferrihydrite,
150 goethite, and hematite) were conducted with 10 mM $NaNO_3$ background electrolyte in glass tubes
151 (Ding et al., 2019). The desired reaction pH values (i.e., 3, 6.5, and 9) were adjusted with 0.1 M
152 HCl and 0.1 M NaOH. Each experiment was conducted in triplicates, and thus the sample numbers
153 in batch experiments were 125. The suspensions were horizontally shaken on a shaking table (200
154 rpm, 25 °C) for 24 h to reach equilibrium under dark condition. After that, the samples were
155 centrifuged at 6000 rpm for 10 min and filtered through 0.45 μm membranes. The filtered
156 supernatants were collected and stored at 4 °C before UV-vis spectrum measurement, TOC
157 analysis, FT-ICR MS measurement, and toxicogenomics assay. Each experiment was conducted
158 in triplicates to increase the statistical power for data analysis. The zeta potentials of iron
159 oxyhydroxides before and after HDOM adsorption were determined over a range of pH (2-10) to
160 obtain their isoelectric points (IEP). After sorption, the iron oxyhydroxides were also collected and
161 lyophilized for FTIR (Nicolet iZ10, Thermo Fisher Scientific, US) and XPS (Escalab 250Xi,
162 Thermo Fisher Scientific, US) analysis to study the structures and functional groups of iron
163 oxyhydroxides and HDOM as well as their interactions. The detailed procedures are described in
164 the Supporting Information.

2.3. FT-ICR MS measurement and data analysis

HDOM samples before and after iron oxyhydroxide sorption were purified and condensed by solid phase extraction (SPE) using Agilent Bond Elute PPL cartridge (500 mg, 6 mL) (Kellerman et al., 2015). The molecular composition of HDOM was analyzed using an FT-ICR MS (Solarix, Bruker Daltonik GmbH, Germany) equipped with a 7 T superconducting magnet, which was operated with an electrospray ionization (ESI) source in negative mode. A same instrument parameter and detection limit were employed for each measurement to facilitate the maximum comparability among samples. Ultrahigh resolution mass spectra with the range of 100-1000 mass-to-charge ratio (m/z) were acquired and then internally recalibrated with known CHO-homologous series of natural organic matter (m/z = 200-600 with >200 mass calibration points) using Bruker Daltonics Data Analysis 4.0 (Gao et al., 2021). Peaks with signal-to-noise ratio (S/N) > 6 were identified as potential target molecules, which were exported for formula assignments. Herein, molecular formulas were assigned using an in-house MATLAB routine (Fu et al., 2020b), with elemental composition of $C_{3\text{-}50}H_{5\text{-}100}O_{1\text{-}30}N_{0\text{-}2}S_{0\text{-}2}$ and elemental ratios of hydrogen-to-carbon (H/C) ≤ 2.0 and oxygen-to-carbon (O/C) ≤ 1.2. Formulas assignments were considered valid if mass error for a given chemical formula between measured mass and theoretical mass was less than 1 ppm, following by double check with seven golden rules (Kind and Fiehn, 2007).

Based on the identified formulas, the key parameters for data analysis were determined according to prior literatures: H/C ratio and O/C ratio, values for constructing van Krevelen diagram (Kim et al., 2003); double bond equivalence (DBE) to estimate number of double bonds or rings in a given molecule (Stenson et al., 2003); aromaticity index (AI), a reference for the degree of aromatic and condensed aromatic structures (Koch and Dittmar, 2006); nominal

oxidation state of carbon (NOSC) to assess the potential redox capacity of each molecule (Fu et al., 2020a); Kendrick mass and Kendrick mass defect (KMD) in order to identify COO homologous series (Hughey et al., 2001). Furthermore, the calculated H/C ratio and AI cutoffs were applied to divided compounds into four groups as follow (Kellerman et al., 2015): aliphatic compounds ($1.5 \leq H/C \leq 2.0$), highly unsaturated and phenolic compounds ($H/C < 1.5$ and $AI \leq 0.50$), vascular plant-derived polyphenols ($0.5 < AI \leq 0.66$), and combustion-derived condensed polycyclic aromatics ($AI > 0.66$). The detailed calculation processes are described in the Supporting Information.

2.4. Toxicogenomics bioassay

The samples of HDOM before and after sorption by iron oxyhydroxides were subjected to the genotoxicity assessment. Given the correlation analysis between genotoxicity profiles and adsorbed molecules, the initial concentration of HDOM was consistent with FT-ICR MS measurement (i.e., 10 mg-C/L). After sorption, the retained molecules were enriched using SPE method, and kept at 4 °C in the dark. The samples were diluted to same values of initial concentration before genotoxicity assay (i.e., 10 mg-C/L). Details of sample preparation and test process are presented in the Supporting Information. In this study, we employed a developed Transcriptional Effect Level Index (TELI) profiling analysis using a green fluorescent protein (GFP) fused whole-cell array of *Escherichia coli* (*E. coli*) K12 MG1655 to conduct a toxicogenomics-based toxicity assessment, which can convert the information-rich toxicogenomic data into integrated and quantitative endpoints (Gou et al., 2011). The selected cell-library with transcriptional GFP fusions monitors the promoter activities of genes associated with various known cellular stress response pathways (e.g., oxidative stress, protein stress, membrane stress

general stress, and DNA stress) and other specific functions (Gou et al, 2014). The selected stress genes and their main functions are presented in Table S1. More detailed calculation procedures are presented in the Supporting Information.

2.5. Statistical analysis

All experiments and relevant measurements were conducted in triplicates to increase the statistical power for data analysis. Data of genotoxicity between triplicated treatments were statistically analyzed using a one-way ANOVA in SPSS 25 software. A difference was considered significant at $P < 0.05$.

3. Results and discussion

3.1. Adsorption of HDOM on iron oxyhydroxides

The adsorption isotherms for HDOM on hematite, goethite, and ferrihydrite at pH 6.5 are presented in Fig. 1a, which were well fitted using the Freundlich and Langmuir models ($R^2 > 0.98$) with fitting parameters summarized in Tables S2 and S3. It can be observed that the sorption of HDOM on three iron oxyhydroxide all exhibited nonlinearities (Table S2). Among these iron oxyhydroxides, ferrihydrite displayed the highest adsorption capacity to HDOM with the value of maximum adsorption capacity (q_m) was 34.55 mg-C/g, which was higher than those of goethite (30.60 mg-C/g) and hematite (29.14 mg-C/g) (Table S3). Such values were comparable to the adsorption capacity of biochar-derived DOM on iron oxyhydroxides, but greatly lower than that of natural organic matter (Liu et al., 2019; Zhang et al., 2020), which might be related the unique molecular properties (e.g., hydrophobicity and aromaticity) of HDOM. Specific UV absorbance at 254 nm ($SUVA_{254}$) was calculated to evaluate the relative aromaticity of DOM (Maizel and

234 Remucal, 2017). Fig. 1b shows that the $SUVA_{254}$ value of HDOM significantly decreased from
235 ~1.5 to ~0.2-0.9 (L mg-C^{-1} m^{-1}) after sorption on iron oxyhydroxides, indicating the molecular
236 fractionation between aromatic and non-aromatic components. In addition, ferrihydrite exhibited
237 the most evident adsorption for aromatic molecules compared with goethite and hematite. The
238 adsorption capacity of three iron oxyhydroxides to HDOM was consistent with the trend of their
239 specific surface areas (i.e., 236.1, 40.9, and 4.6 m^2/g for ferrihydrite, goethite, and hematite,
240 respectively) (Fig. S2). Such result was consistent with a previous study that ferrihydrite exhibited
241 higher affinity to peat-derived DOM than did goethite or lepidocrocite (Lv et al., 2016). Moreover,
242 the HDOM sorption on iron oxyhydroxide decreased with the pH increasing from 3 to 9 (Fig. S3),
243 which could be attributed to the variation of surface charge of iron oxyhydroxide and HDOM. As
244 illustrated in Fig. S4, the IEP for hematite, goethite, and ferrihydrite were 5.0, 8.5, and 6.9,
245 respectively, while the HDOM remained negative charged under the tested pH (2-10). Hence, as
246 pH increased from 3 to 9, the interaction between iron oxyhydroxides and HDOM transformed
247 from electrostatic attraction to electrostatic repulsion, and thereby resulted in declining sorption,
248 which was in line with the adsorption of soil organic matter on allophane and ferrihydrite (Ding et
249 al., 2019; Liu et al., 2019).
250
251 *3.2. Variation of surface functional groups for iron oxyhydroxides caused by HDOM sorption*
252 The changes of surface functionality for three iron oxyhydroxides before and after HDOM
253 sorption are characterized with FTIR and XPS analysis (Figs. 1c and d). For the virgin hematite,
254 the typical adsorption peaks at 429 and 525 cm^{-1} were attributed to bending vibration of Fe-O band
255 (Chen et al., 2022). Typical peaks at 641, 798, and 904 cm^{-1} for goethite belonged to Fe-O/Fe-O-
256 H bending, while Fe-O/Fe-O-H bending for ferrihydrite appeared at 1382 and 1465 cm^{-1}. After

adsorbing HDOM by hematite and goethite, these characteristic peaks for Fe-O/Fe-O-H bending remained stable, while new peaks occurred at 1045, 1641, and 3394 cm^{-1} corresponding to stretching vibrations of C-O-C, C=O, and -OH, respectively (Fig. 1c) (Liu et al., 2020; Lv et al., 2016). However, the characteristic peaks of ferrihydrite after the HDOM sorption changed in the intensities and positions to some extents. The intensities of the peaks at 1382 and 1465 cm^{-1} for Fe-O bending decreased due to the coordination interaction between ferrihydrite and HDOM molecules, which was consistent with the FTIR spectrum of ferrihydrite-biochar derived DOM complex (Zhang et al., 2020). These emerging peaks presented on three iron oxyhydroxides after HDOM sorption were all in line with FTIR spectrum of the original HDOM (Fig. S5 and Table S4), indicating that various HDOM component were adsorbed by three iron oxyhydroxides.

XPS measurement was further conducted to reveal the discrepancy of the adsorbed HDOM component caused by iron oxyhydroxides (Figs. 1d, S6, and Table S5). The overall results showed that the contents of C/O/N on iron oxyhydroxides obviously increased after HDOM sorption, and followed the order of ferrihydrite > goethite > hematite (Fig. S6 and Table S5). Moreover, the high-resolution C1s spectra was analyzed and three main functional groups (i.e., -C-C/-C=C (284.86 eV), C-O-(C, H) (286.45 eV), and HO-C=O (288.13 eV)) were identified (Fig. 1d) (Zhang et al., 2020). The molecules containing functional groups of -C-C/-C=C were the primary component (~60%) on the goethite and hematite after HDOM sorption, whose contents were significantly higher than those of C-O-(C, H) (~30%) and HO-C=O (~10%). Conversely, the relative content of C-O-(C, H) was the greatest (~52%) on the ferrihydrite surface after HDOM sorption, and followed by -C-C/-C=C (40%) and HO-C=O (9%) (Table S5). Such phenomenon demonstrated that the less aromatic molecules with more polar groups were preferentially retained by goethite and hematite, while ferrihydrite preferentially absorbed unsaturated polyphenols and

carboxylic compounds. The selective adsorption of HDOM on iron oxyhydroxides might mainly be attributed to their physicochemical properties. Amorphous ferrihydrite dominated by (001/021)-like faces have abundant singly coordinated surface hydroxy, which could bond to reactive oxygen-containing functional groups (e.g., hydroxy and carboxyl) via ligand exchange surface complexation and form innersphere complex (Buck et al., 2012; Gu et al., 1994). However, goethite and hematite possess stable crystal structure, low specific surface area, and less surface hydroxy, electrostatic interaction, hydrogen bonding, and van der Waals forces were recognized as main mechanisms for HDOM adsorption and exhibited higher affinity to aliphatic polar molecules (Han et al., 2021; Lv et al., 2018; Wang et al., 2019). Therefore, it can be inferred by combining FTIR and XPS analyses that iron oxyhydroxides exhibited the selective sorption and fractionation for HDOM, but the details of molecular fractionations need to be further characterized for the residue HDOM after sorption using FT-ICR MS.

3.3. Molecular fractionation of HDOM induced by iron oxyhydroxides

The remarkable advances in high-resolution mass spectrum make it possible to reveal the evolution of DOM composition at molecular level. In this study, we used FT-ICR MS to reveal the molecular fractionation of HDOM on the iron oxyhydroxides. By using H/C ratio and AI cutoffs, all the detected HDOM molecules presented in the van Krevelen diagram were divided into four groups: the aliphatic compounds (Group I), the highly unsaturated and phenolic compounds (Group II), the vascular plant-derived polyphenols (Group III), and the combustion-derived condensed polycyclic aromatics (Group IV) (Fig. 2). For the original HDOM, the highest proportion of the compounds was the highly unsaturated and phenolic compounds (74%), which significantly exceeded those of aliphatic compounds (16%), polyphenols (9%), and condensed

303 polycyclic aromatics (0.5%) (Fig. 2a). After adsorbed on ferrihydrite, nearly 70% of the total
304 compounds disappeared in the residual HDOM, in which Group I, Group II, Group III, and Group
305 IV accounted for 10%, 78%, 11%, and 0.3% of total adsorbed molecules, respectively (Figs. 2d
306 and S7). However, only 27% and 58% of HDOM molecules were adsorbed by hematite and
307 goethite, respectively. Meanwhile, the proportion of Group I in total adsorbed molecules by
308 hematite and goethite were greatly higher than those of ferrihydrite (~19% vs 10%), but Group II
309 and Group III was less adsorbed by hematite and goethite compared with ferrihydrite (~72% vs
310 78% for Group II; ~8% vs 11% for Group III) (Figs. 2b, 2c and S7). These results indicated that
311 the three iron oxyhydroxides exhibit variations in the adsorption fractionation of HDOM, which
312 might mainly due to their different physicochemical properties. Amorphous ferrihydrite is
313 dominated by (001/021)-like faces and possess large specific surface area and high singly
314 coordinated surface hydroxy (≡FeOH) (Jambor and Dutrizac, 1998), while goethite is dominated
315 by (110/100)-like faces contributes to triply coordinated (≡Fe_3OH) surface hydroxyl. Previous
316 study demonstrated that the singly coordinated (≡FeOH) groups exhibited a higher affinity to
317 organic substances than the triply coordinated (≡Fe_3OH) surface hydroxyls, leading to different
318 molecular fractionation of HDOM on ferrihydrite and goethite (Liu et al., 2014). Hematite exhibits
319 less surface adsorption sites, resulting in the weakest adsorption fractionation of HDOM. Such
320 selective sorption of those unsaturated phenolic compounds, polyphenols, and organic acids with
321 high O content in HDOM by iron oxyhydroxides further resulted in an increase in H/C, and
322 decrease of molecular weight (M_W), O/C, DBE, and NOSC of the residual HDOM in the solution
323 (Table S6).

324 In addition, van Krevelen plots of HDOM molecules in Figs. S8 and S9 showed the positive
325 correlation between O number and DBE values for the iron oxyhydroxide-adsorbed molecules,

which manifested that the oxygen content and the unsaturation level of various compounds in HDOM might play important roles in governing HDOM adsorption behavior. Plots of DBE values versus O numbers in the molecular formulas of HDOM before and after adsorption on iron oxyhydroxides were therefore investigated (Fig. 3). Most of molecules in the original HDOM contained 3-20 oxygen atoms with DBE ranging from 1-25. Hematite represented little contribution to the adsorption of molecules with special oxygen number or DBE values (Fig. 3a), while these compounds with O atoms over 17 or DBE value above 22 basically disappeared in the residual HDOM after goethite sorption (Fig. 3b). In particular, almost all the compounds containing over 14 O atoms or with DBE values above 17 were adsorbed by ferrihydrite (Fig. 3c). All above results indicated that that the HDOM components with higher O contents and DBE values (e.g., carboxylic molecules) were preferentially adsorbed by iron oxyhydroxides. Therefore, COO-scale KMD analysis was employed to probe the roles of -COO groups in the adsorptive fractionation of HDOM on iron oxyhydroxide surface. The molecules which share the same KMD value are those in a COO homologous series or with an identical core structure. As shown in Figs. 4a-c, the adsorption of specific molecules increased with the increase of COO number, which suggested that the molecules with more COO groups were preferentially adsorbed on iron oxyhydroxides. Particularly, ferrihydrite represented the most dominant adsorption for the molecules with higher M_W and COO number. Such results suggested that the molecule acidity (e.g., COO groups) may control the DOM adsorptive fractionation on iron oxyhydroxides, possibly through the surface ligand exchange involving carboxylic groups. Similar phenomenon was also observed for the adsorption of soil organic matter on ferrihydrite and allophane (Ding et al., 2019; Lv et al., 2014).

3.4. Evolution in molecular toxicity transcriptomic fingerprints of HDOM induced by molecular fractionation

Previous studies mainly investigated the molecular fractionation of DOM on iron oxyhydroxides (Liu et al., 2019; Lv et al., 2014; Wang et al., 2019; Ye et al., 2023), while its effects on biotoxicity evolution at genetic level has been neglected. TELI, a quantitative endpoint for toxicogenomics-based toxicity assay, was employed to investigate the genotoxicity of HDOM before and after adsorption on iron oxyhydroxides through various damage pathways (i.e., oxidative, protein, membrane, general, and DNA stresses) to microbial cells. As shown in Fig. 5, the altered gene expression induced by original HDOM and post-adsorption HDOM components exhibited completely different profiles. Overall, lots of gene expressions (e.g., *gst*, *marR*, *flgM*, *ssrA*, *mutT*, and *nfo*) induced by HDOM were changed by iron oxyhydroxide sorption as reflected by TELI heatmap (Fig. 5a). Based on statistical analysis, the total stresses were significantly induced by original HDOM (Fig. 5b), which was comparable to the heavy metals (e.g., Pb^{2+}, Cu^{2+}, and Ni^{2+}), and organic pollutants (e.g., trichloroacetic acid, erythromycin, and bisphenol A) at similar concentration levels (Gou et al., 2011; Gou et al., 2010; Gou et al., 2014; Liu et al., 2023; Zheng et al., 2020), indicating the higher genotoxicity of original HDOM to microbes. The total stresses were also significantly induced by original HDOM molecules after hematite sorption, while HDOM molecules after goethite and ferrihydrite sorption made no significant genotoxicity to microbe ($P < 0.05$) (Fig. 5b). Subsequently, the transcriptional level response for each stress category was further quantified by calculating their individual TELI values. The results showed that all damage pathways were significantly induced by original HDOM, while iron oxyhydroxide sorption reduced the responses in oxidative, membrane, and DNA stresses. In detail, the original HDOM and HDOM after hematite sorption both exhibited significantly higher TELI values for

oxidative and membrane stress, while HDOM molecules after goethite and ferrihydrite sorption represent no obvious toxicity compared with the control group (Figs. 5c and e). Notably, there was no significant difference observed in protein and general stress between HDOM samples before and after sorption by iron oxyhydroxide (Figs. 5d and f), whereas, all iron oxyhydroxide sorption remarkably reduced DNA stress with $P < 0.01$ (Fig. 5g).

To reveal genetic level information of oxidative, membrane, and DNA stresses induced by various HDOM samples before and after adsorption on iron oxyhydroxides, more in-depth examination of gene activities ($TELI_{gene}$ >1.5) for stress response pathways was conducted (Fig. S10). Fig. S10a showed the altered gene expression in selected oxidative stress biomarker genes, which are involved in defending against oxidative stress and scavenging intracellular oxidative radicals (e.g., •OH, $O_2^{\bullet-}$ and $^1O_2$) (Keseler et al., 2011). Genes (i.e., *sodA*, *katE*, and *aphC*) which contributed to the synthesis of enzymes converting superoxide radicals to water, scavenging H_2O_2, and quenching hydroperoxide, respectively, were all significantly upregulated when exposed to original HDOM. In addition, *gst* gene coding the synthesis of glutathione s-transferases which play an important role in detoxification by catalyzing the conjugation of many hydrophobic and electrophilic compounds with reduced glutathione (Hilliou et al., 2021), was also greatly upregulated by original HDOM (Fig. 5a). However, these genes were not activated or downregulated when exposure to HDOM after adsorption on iron oxyhydroxides (Figs. 5a and S10a). Similar phenomenon was also observed for DNA stress in which most of genes related with SOS response (e.g., *recA*), base excision repair (e.g., *mutT* and *nfo*), nucleotide excision repair (e.g., *uvrA*), mismatch repair (e.g., *ssb*), and double-strand break repair (e.g., *recA* and *recN*) were overexpressed by original HDOM, while none of them were activated when exposure to HDOM after adsorption on iron oxyhydroxides (Fig. S10b). Different from oxidative and DNA stresses,

membrane stress is less affected by adsorption of iron oxyhydroxides (Fig. S10c). Genes were classified into several subcategories based on the membrane structure and function, including energy (*sdhC* and *cyoA*), multidrug efflux (*emrA*, *emrE*, and *marR*), cell wall and membrane structure (*san*, *bacA*, and *dacB*), and flagella (*motA* and *flgM*). All these genes were upregulated by original HDOM, and many genes related to multidrug efflux and the cell membrane structure and envelope (e.g., *emrA*, *emrE*, *san*, *bacA*, and *dacB*) continuously kept activated by HDOM molecules after adsorption on iron oxyhydroxides, only genes connected with energy (*sdhC* and *cyoA*), and flagella (*motA* and *flgM*) were not activated when exposure to HDOM after adsorption on goethite and ferrihydrite. Additionally, *ssrA* gene related with the synthesis of specific proteases which responsible for degradation of organic compounds (Fritze et al., 2020), was greatly upregulated by original HDOM, while failed to be activated by HDOM molecules after adsorption on iron oxyhydroxides (Fig. 5a).

3.5. Correlation between molecular fractionation and genotoxicity profiles of HDOM

Spearman's correlation between the FT-ICR MS molecular parameters and TELI values was conducted to reveal the effects of molecular fractionation on genotoxicity and ecological risks of HDOM. As showed in Fig. S11, the key molecular parameters (i.e., Mass, O/C, and DBE) were significantly positive with the values of $TELI_{total}$, $TELI_{oxidative}$, $TELI_{membrane}$, and $TELI_{DNA}$ ($P < 0.05$), which indicated that the compounds with higher M_W, O content, and unsaturated groups tended to induce genotoxicity including oxidative, membrane, and DNA stresses. HDOM molecules with higher MW, O content, and unsaturated groups mainly contained aromatic structures, hydroxy, and carboxyl, which could be classified into phenols, polyphenols, and organic acids (Ennis et al., 2012). Such molecules were reported to have higher affinity to lipid

418 compounds and higher biotoxicity to organisms (Hao et al., 2018). Therefore, when contacted with
419 microbes, these HDOM molecules might adhere to bacterial surface or get inside cell, and induce
420 the production of reactive oxygen species (e.g., •OH, $O_2^{\bullet-}$ and $^1O_2$) and trigger oxidative stress.
421 The overproduction of reactive oxygen species could further attack cell membrane and even DNA
422 chains, and consequently induced more serious membrane damage and DNA stress (Gou et al.,
423 2010; Gou et al., 2011; Liu et al., 2023). Compared with natural organic matters, HDOM had
424 higher M_W and DBE values (Table S7), and therefore exhibited a high potential genotoxicity to
425 microbes (Fig. 5 and Table S8). Such results could explain why the selective adsorption of
426 unsaturated phenolic compounds and polyphenols with high O content by iron oxyhydroxides
427 significantly reduced the genotoxicity of HDOM (Figs. 2-5). Noticeably, the genotoxicity of
428 HDOM was remarkably weaken after iron oxyhydroxide adsorption, indicating that these toxic
429 compounds were retained in iron oxyhydroxides. As discussed above, such toxic compounds might
430 adhere to bacterial surface or even get inside cell, and consequently result in the oxidative stress
431 of microorganism (Fig. 5c), and the overproduction of ROS further induced more serious
432 membrane stress and DNA damage which involve almost all the DNA repair pathways (e.g., base
433 excision repair, excision repair, mismatch repair, double-strand break repair) (Figs. 5c-g and S10).
434 Additionally, the increased possibility of base mismatch caused by multi-repair mechanisms might
435 result in gene mutation and further increase the environmental risks (Garcia et al., 2020; Maiques
436 et al., 2006). Therefore, selective adsorption of toxic chemicals by iron oxyhydroxides may change
437 the microbial community of surrounding soil and even provide selective pressure to pathogens
438 (Cheng et al., 2023), imposing a potential threat to soil ecosystems (Fig. 6). On the other hand, the
439 remaining molecules with lower biotoxicity would flow into aquatic environments and can provide
440 carbon source for microorganism growth, and thus affect microbial community structure and even

the ecological functions of aquatic ecosystems (Fig. 6). Furthermore, the variation of gene expressions (e.g., *gst*, *marR*, and *ssrA*) associated with detoxification and drug resistance induced by HDOM before and after iron oxyhydroxide sorption not only disturbed the microbial growth but also affected transformation of environmental pollutants, imposing a potential threat to terrestrial and aquatic ecological functions. Therefore, future studies are needed to study the ecological effects of HDOM to soil and water environments with consideration of the sorption by soil minerals especially for iron oxyhydroxides.

4. Conclusions

Hydrochar is a kind of functional material with application value in the field of soil remediation, yet the environmental process and potential risks of hydrochar-based DOM at molecular level at soil-water interface with consideration of soil minerals remain largely unknown. Using ESI-FT-ICR MS and TELI-based toxicity assessment approach, this study addressed the sorption fractionation of HDOM on iron oxyhydroxides and its influence to genotoxicity evolution at molecular level. Results demonstrated that HDOM molecules with high M_W and high contents of unsaturated oxidized or aromatic structures (e.g., unsaturated phenolic compounds, polyphenols, and organic acids) were preferentially absorbed by iron oxyhydroxides, while aliphatic molecules and poorly oxygenated compounds (e.g., hydrocarbon, phenols, and alcohols) were retained in water phase. Such selectively adsorption process further leaded to the mitigation of genotoxicity (especially for oxidative, membrane, and DNA stresses) in residual HDOM as confirmed by the decreased TELI values. Notably, poorly crystalline ferrihydrite exhibited more pronounced molecular fractionation and genotoxicity reduction of HDOM than did goethite or hematite. Overall, iron oxyhydroxides affect the distribution of HDOM molecules between soil and water

phase, which might potentially disturb the microbial community structure, transformation of environmental pollutants, and even the ecological function of both terrestrial and aquatic ecosystems through mediating genotoxicity evolution. Therefore, future studies are needed to study the ecological effects of HDOM to soil and water environments considering the sorption by iron oxyhydroxides and to optimize the hydrothermal carbonization operation for generating hydrochar with less toxicity.

CRediT authorship contribution statement

Yan-Jun Liu: Conceptualization, Data curation, Formal analysis, Investigation, Methodology, Software, Visualization, Writing-original draft. **He-Yun Yang**: Conceptualization, Data curation, Formal analysis, Software, Visualization. **Shu-Xian Gao**: Methodology, Software, Visualization. **Zheng-Hao Li**: Conceptualization, Resources, Writing-review & editing. **Yan-Yun Hu**: Investigation, Methodology. **Xing Zheng**: Conceptualization, Resources, Writing-review & editing. **Guo-Ping Sheng**: Conceptualization, Funding acquisition, Supervision, Writing -review & editing.

Declaration of competing interest

The authors declare that they have no known competing financial interests or personal relationships that could have appeared to influence the work reported in this paper.

Acknowledgements

The authors wish to thank the National Natural Science Foundation of China (51821006, and 52200110), the China Postdoctoral Science Foundation (2022M723035), and the Fundamental

Research Funds for the Central Universities for the support of this study.

Appendix. Supplementary material

The Supplementary material that contains relevant data to this article can be found at Appendix A.

Data availability

Data will be made available on request.

References

Buck, K.N., Moffett, J., Barbeau, K.A., Bundy, R.M., Kondo, Y., Wu, J., 2012. The organic complexation of iron and copper: an intercomparison of competitive ligand exchange-adsorptive cathodic stripping voltammetry (CLE-ACSV) techniques. Limnol. Oceanogr-Meth. 10, 496-515.

Chen, W.P., Huangfu, X.L., Xiong, J.M., Liu, J.C., Wang, H.N., Yao, J.N., Liu, H.X., He, Q., Ma, J., Liu, C.H., Chen, Y., 2022. Retention of thallium(I) on goethite, hematite, and manganite: Quantitative insights and mechanistic study. Water Res. 221, 118836.

Cheng, Y.D., Wang, X., Zhao, L.W., Zhang, X., Kong, Q.X., Li, H., You, X.W., Li, Y.Q., 2023. Wheat straw pyrochar more efficiently decreased enantioselective uptake of dinotefuran by lettuce and dissemination of antibiotic resistance genes than hydrochar in an agricultural soil. Sci. Total Environ. 880, 163088.

Ding, Y., Lu, Y., Liao, P., Peng, S.M., Liang, Y.Z., Lin, Z., Dang, Z., Shi, Z.Q., 2019. Molecular fractionation and sub-nanoscale distribution of dissolved organic matter on allophane. Environ. Sci. Nano 6 (7), 2037-2048.

Ennis, C.J., Evans, A.G., Islam, M., Ralebitso-Senior, T.K., Senior, E., 2012. Biochar: carbon sequestration, land remediation, and impacts on soil microbiology. Crit. Rev. Environ. Sci. Technol. 42 (22), 2311-2364.

Feng, X.D., Siegel, M.M., 2007. FT-ICR MS applications for the structure determination of natural products. Anal. Bioanal. Chem. 389 (5), 1341-1363.

Fritze, J., Zhang, M., Luo, Q., Lu, X., 2020. An overview of the bacterial *ssrA* system modulating intracellular protein levels and activities. Appl. Microbiol. Biotechnol. 104 (12), 5229-5241.

Fu, Q.L., Fujii, M., Kwon, E., 2020a. Development and application of a high-precision algorithm

519 for nontarget identification of organohalogens based on ultrahigh-resolution mass
520 spectrometry. Anal. Chem. 92 (20), 13989-13996.
521 Fu, Q.L., Fujii, M., Riedel, T., 2020b. Development and comparison of formula assignment
522 algorithms for ultrahigh-resolution mass spectra of natural organic matter. Anal. Chim. Acta.
523 1125, 247-257.
524 Gao, S.X., Zhang, X., Fan, W.Y., Sheng, G.P., 2021. Molecular insight into the variation of
525 dissolved organic phosphorus in a wastewater treatment plant. Water Res. 203, 117529
526 Garcia, J., Jesus Garcia-Galan, M., Day, J.W., Boopathy, R., White, J.R., Wallace, S., Hunter, R.C.,
527 2020. A review of emerging organic contaminants (EOCs), antibiotic resistant bacteria (ARB),
528 and antibiotic resistance genes (ARGs) in the environment: Increasing removal with wetlands
529 and reducing environmental impacts. Bioresour. Technol. 307, 123228.
530 Ge, M., Wang, B., Chen, B., Xie, H., Sun, H., Sun, K., Feng, Y., 2024. Hydrochar and its dissolved
531 organic matter aged in a 30-month rice-wheat rotation system: Do primary aging factors alter
532 at different stages? Environ. Sci. Technol. 58 (6), 3019-3030.
533 Gou, N., Gu. A.Z., 2011. A new transcriptional effect level index (TELI) for toxicogenomics-based
534 toxicity assessment. Environ. Sci. Technol. 45 (12), 5410-5417.
535 Gou, N., Onnis-Hayden, A., Gu, A. Z., 2010. Mechanistic toxicity assessment of nanomaterials by
536 whole-cell-array stress genes expression analysis. Environ. Sci. Technol. 44 (15), 5964-5970.
537 Gou, N., Yuan, S. H., Lan, J.Q., Gao, C., Alshawabkeh, A.N., Gu, A.Z., 2014. A quantitative
538 toxicogenomics assay reveals the evolution and nature of toxicity during the transformation
539 of environmental pollutants. Environ. Sci. Technol. 48 (15), 8855-8863.
540 Gu, B.H., Schmitt, J., Chen, Z.H., Liang, L.Y., McCarthy, J.F., 1994. Adsorption and desorption
541 of natural organic matter on iron oxide: Mechanisms and models. Environ. Sci. Technol. 28(1),

542 38-46.
543 Han, L., Yang, Y., Sun, K., Zhang, B., Chen, Y., Fang, L., Xing, B., 2021. Different mechanisms
544 driving the preferential adsorption of dissolved organic matter by goethite and
545 montmorillonite. Chem. Geol. 585, 120560.
546 Hanna, K., 2007. Sorption of two aromatic acids onto iron oxides: Experimental study and
547 modeling. J. Colloid Interface Sci. 309 (2), 419-428.
548 Hao, S.L., Zhu, X.D., Liu, Y.C., Qian, F., Fang, Z., Shi, Q., Zhang, S.C., Chen, J.M., Ren, Z.J.,
549 2018. Production temperature effects on the structure of hydrochar-derived dissolved organic
550 matter and associated toxicity. Environ. Sci. Technol. 52 (13), 7486-7495.
551 Hilliou, F., Chertemps, T., Maibeche, M., Le Goff, G., 2021. Resistance in the genus *Spodoptera*:
552 Key insect detoxification genes. Insects 12 (6), 544.
553 Huang, M., Li, Z., Huang, B., Luo, N., Zhang, Q., Zhai, X., Zeng, G., 2018. Investigating binding
554 characteristics of cadmium and copper to DOM derived from compost and rice straw using
555 EEM-PARAFAC combined with two-dimensional FTIR correlation analyses. Journal of
556 Hazardous Materials 344, 539-548.
557 Hughey, C.A., Hendrickson, C.L., Rodgers, R.P., Marshall, A.G., Qian, K.N., 2001. Kendrick mass
558 defect spectrum: A compact visual analysis for ultrahigh-resolution broadband mass spectra.
559 Anal. Chem. 73 (19), 4676-4681.
560 Jambor, J.L., Dutrizac, J.E., 1998. Occurrence and constitution of natural and synthetic ferrihydrite,
561 a widespread iron oxyhydroxide. Chem. Rev. 98(7), 2549-2585.
562 Kellerman, A.M., Kothawala, D.N., Dittmar, T., Tranvik, L.J., 2015. Persistence of dissolved
563 organic matter in lakes related to its molecular characteristics. Nat. Geosci. 8 (6), 454-452.
564 Keseler, I.M., Collado-Vides, J., Santos-Zavaleta, A., Peralta-Gil, M., Gama-Castro, S., Muniz-

Rascado, L., Bonavides-Martinez, C., Paley, S., Krummenacker, M., Altman, T., Kaipa, P., Spaulding, A., Pacheco, J., Latendresse, M., Fulcher, C., Sarker, M., Shearer, A.G., Mackie, A., Paulsen, I., Gunsalus, R.P., Karp, P.D., 2011. EcoCyc: a comprehensive database of Escherichia coli biology. Nucleic Acids Res. 39, D583-D590.

Kim, S., Kramer, R.W., Hatcher, P.G., 2003. Graphical method for analysis of ultrahigh-resolution broadband mass spectra of natural organic matter, the van Krevelen diagram. *Anal. Chem.* 75 (20), 5336-5344.

Kind, T., Fiehn, O., 2007. Seven golden rules for heuristic filtering of molecular formulas obtained by accurate mass spectrometry. BMC Bioinformatics 8, 105.

Koch, B.P., Dittmar, T., 2006. From mass to structure: an aromaticity index for high-resolution mass data of natural organic matter. Rapid Commun. Mass Spectrom. 20 (5), 926-932.

Lalonde, K., Mucci, A., Ouellet, A., Gelinas, Y., 2012. Preservation of organic matter in sediments promoted by iron. Nature 483 (7388), 198-200.

Liu, H.B., Chen, T.H., Frost, R.L., 2014. An overview of the role of goethite surfaces in the environment. Chemosphere 103, 1-11.

Liu, M.Q., Ding, Y., Peng, S.M., Lu, Y., Dang, Z., Shi, Z.Q., 2019. Molecular fractionation of dissolved organic matter on ferrihydrite: effects of dissolved cations. Environ. Chem. 16(2), 137-148.

Liu, Y.J., Yang, H.Y., Hu, Y.Y., Li, Z.H., Yin, H., He, Y.T., Zhong, K.Q., Yuan, L., Zheng, X., Sheng, G.P., 2023. Face mask derived micro(nano)plastics and organic compounds potentially induce threat to aquatic ecosystem security revealed by toxicogenomics-based assay. Water Res. 242, 120251.

Liu, Y.J., Huang, Z.Q., Zhou, J.N., Tang, J., Yang, C., Chen, C.Y., Huang, W.L., Dang, Z., 2020.

588 Influence of environmental and biological macromolecules on aggregation kinetics of
589 nanoplastics in aquatic systems. Water Res. 186, 116316.
590 Luo, L., Wang, J.X., Lv, J.T., Liu, Z.G., Sun, T.R., Yang, Y., Zhu, Y.G., 2023. Carbon sequestration
591 strategies in soil using biochar: advances, challenges, and opportunities. Environ. Sci.
592 Technol. 57 (31), 11357-11372.
593 Lv, J.T., Zhang, S.Z., Wang, S.S., Luo, L., Cao, D., Christie, P., 2016. Molecular-scale investigation
594 with ESI-FT-ICR-MS on fractionation of dissolved organic matter induced by adsorption on
595 iron oxyhydroxides. Environ. Sci. Technol. 50 (5), 2328-2336.
596 Lv, J.T., Miao, Y., Huang, Z., Han, R., Zhang, S., 2018. Facet-mediated adsorption and molecular
597 fractionation of humic substances on hematite surfaces. Environ. Sci. Technol. 52(20), 11660-
598 11669.
599 Magdziarz, A., Wilk, M., Wadrzyk, M., 2020. Pyrolysis of hydrochar derived from biomass -
600 Experimental investigation. Fuel 267, 117246.
601 Maiques, E., Ubeda, C., Campoy, S., Salvador, N., Lasa, I., Novick, R.P., Barbe, J., Penades, J.R.,
602 2006. beta-lactam antibiotics induce the SOS response and horizontal transfer of virulence
603 factors in Staphylococcus aureus. J. Bacteriol. 188 (7), 2726-2729.
604 Maizel, A.C., Remucal, C.K., 2017. The effect of advanced secondary municipal wastewater
605 treatment on the molecular composition of dissolved organic matter. Water Res. 122, 42-52.
606 Melton, E.D., Swanner, E.D., Behrens, S., Schmidt, C., Kappler, A., 2014. The interplay of
607 microbially mediated and abiotic reactions in the biogeochemical Fe cycle. Nat. Rev.
608 Microbial. 12 (12), 797-808.
609 Mueller, S., Totsche, K.U., Koegel-Knabner, I., 2007. Sorption of polycyclic aromatic
610 hydrocarbons to mineral surfaces. Eur. J. Soil Sci. 58 (4), 918-931.

Ona-Nguema, G., Morin, G., Juillot, F., Calas, G., Brown, G.E., 2005. EXAFS analysis of arsenite adsorption onto two-line ferrihydrite, hematite, goethite, and lepidocrocite. Environ. Sci. Technol. 39 (23), 9147-9155.

Stenson, A.C., Marshall, A.G., Cooper, W.T., 2003. Exact masses and chemical formulas of individual Suwannee River fulvic acids from ultrahigh resolution electrospray ionization Fourier transform ion cyclotron resonance mass spectra. Anal. Chem. 75 (6), 1275-1284.

Sun, K., Han, L.F., Yang, Y., Xia, X.H., Yang, Z.F., Wu, F.C., Li, F.B., Feng, Y.F., Xing, B.S., 2020. Application of hydrochar altered soil microbial community composition and the molecular structure of native soil organic carbon in a paddy soil. Environ. Sci. Technol. 54 (5), 2715-2725.

Wang, Y., Zhang, Z., Han, L., Sun, K., Jin, J., Yang, Y., Yang, Y., Hao, Z., Liu, J., Xing, B., 2019. Preferential molecular fractionation of dissolved organic matter by iron minerals with different oxidation states. Chem. Geol. 520, 69-76.

Wang, P., Ding, Y., Liang, Y.Z., Liu, M.Q., Lin, X.F., Ye, Q.T., Shi, Z.Q., 2021. Linking molecular composition to proton and copper binding ability of fulvic acid: A theoretical modeling approach based on FT-ICR-MS analysis. Geochim. Cosmochim. Acta. 312, 279-298.

Wu, S., Konhauser, K.O., Chen, B.D., Huang, L.B., 2023. “Reactive Mineral Sink” drives soil organic matter dynamics and stabilization. NPJ Mat. Sustain. 3, 1-12.

Xia, L.L., Cao, L., Yang, Y., Ti, C.P., Liu, Y.Z., Smith, P., van Groenigen, K.J., Lehmann, J., Lal, R., Butterbach-Bahl, K., Kiese, R., Zhuang, M.H., Lu, X., Yan, X.Y., 2023. Integrated biochar solutions can achieve carbon-neutral staple crop production. Nat. Food 4 (3), 236-246.

Xiang, L.L., Harindintwali, J.D., Wang, F., Redmile-Gordon, M., Chang, S.X., Fu, Y.H., He, C., Muhoza, B., Brahushi, F., Bolan, N., Jiang, X., Ok, Y.S., Rinklebe, J., Schaeffer, A., Zhu, Y.G.,

Tiedje, J.M., Xing, B.S., 2022. Integrating biochar, bacteria, and plants for sustainable remediation of soils contaminated with organic pollutants. Environ. Sci. Technol. 56 (23), 16546-16566.

Yan, W., Hastings, J.T., Acharjee, T.C., Coronella, C.J., Vasquez, V.R., 2010. Mass and energy balances of wet torrefaction of lignocellulosic biomass. Energy Fuels 24 (9), 4738-4742.

Ye, Y.P., Wang, Z.W., Liu, L.J., Qi, K.M., Xie, X.Y., 2023. Novel insights into the temporal molecular fractionation of dissolved black carbon at the iron oxyhydroxide-water interface. Water Res. 229, 119410.

Zhang, C.B., Wang, Q.J., Qin, R.J., Li, Z.T., Wang, Y., Ke, Z.Z., Ren, G.P., 2023. Natural hematite as low-cost auxiliary material for improving soil remediation by in-situ microbial community. Environ. Sci. Pollut. Res. Int. 30, 84141-84151.

Zhang, P., Liu, A.J., Huang, P., Min, L.J., Sun, H.W., 2020. Sorption and molecular fractionation of biochar-derived dissolved organic matter on ferrihydrite. J. Hazard. Mater. 392, 122260.

Zhang, Z.K., Zhu, Z.Y., Shen, B.X., Liu, L.N., 2019. Insights into biochar and hydrochar production and applications: A review. Energy 171, 581-598.

Zhao, Y., Moore, O.W., Xiao, K.Q., Curti, L., Farina, A.O., Banwart, S.A., Peacock, C.L., 2022. The role and fate of organic carbon during aging of ferrihydrite. Geochim. Cosmochim. Acta. 335, 339-355.

Zheng, X., Liu, T., Guo, M.H., Li, D., Gou, N., Cao, X., Qiu, X.P., Li, X.L., Zhang, Y.Z., Sheng, G.P., Pan, B.C., Gu, A.Z., Li, Z.B., 2020. Impact of heavy metals on the formation and properties of solvable microbiological products released from activated sludge in biological wastewater treatment. Water Res. 179, 115895.

Figure captions

Fig. 1. (a) Adsorption isotherms of HDOM on hematite, goethite, and ferrihydrite (pH 6.5, 10 mM $NaNO_3$). (b) $SUVA_{254}$ of HDOM before and after sorption on hematite, goethite, and ferrihydrite. (c) FTIR spectra of three iron oxyhydroxides before and after HDOM sorption. (d) High-resolution of C1s spectrums with curve-fitting for original HDOM and iron oxyhydroxides-adsorbed HDOM components. Hematite/Goethite/Ferrihydrite-HDOM denote HDOM components adsorbed by hematite, goethite, and ferrihydrite, respectively. rHDOM- Hematite/Goethite/Ferrihydrite denote residual HDOM components after adsorption by hematite, goethite, and ferrihydrite, respectively.

Fig. 2. van Krevelen (VK) diagrams revealed molecular composition of HDOM (a) before and after adsorption on (b) hematite, (c) goethite, (d) ferrihydrite, respectively. Four categories are divided by the aromaticity index (AI) and H/C cutoffs as follow: aliphatic compounds (Group I, $1.5 \leqslant H/C \leqslant 2.0$), highly unsaturated and phenolic compounds (Group II, H/C < 1.5 and $AI \leqslant 0.50$), vascular plant-derived polyphenols (Group III, $0.50 \leqslant AI \leqslant 0.66$), and combustion-derived condensed polycyclic aromatics (Group IV, $AI > 0.66$). Color bar represents the relative abundance of molecules with % unit.

Fig. 3. Plots of Double-bond equivalence (DBE) versus the number of O atoms in molecular formulas of HDOM after adsorption on (a) hematite, (b) goethite, and (c) ferrihydrite, respectively. The black hollow square represents the original HDOM molecules, and the blue, green, and red hollow circles represent the residual HDOM molecules after sorption by

hematite, goethite, and ferrihydrite, respectively.

Fig. 4. Kendrick mass analysis of CHO molecules after sorption by (a) hematite, (b) goethite, and (c) ferrihydrite. Formulas that share the same KMD (COO) value are carboxylation homologs. The black hollow square represents the original HDOM molecules and the blue, green, and red hollow circles represent the residual HDOM molecules after sorption by hematite, goethite, and ferrihydrite, respectively.

Fig. 5. Genotoxicity evolution of HDOM before and after sorption by three iron oxyhydroxides. (a) Heatmap of TELI value for each individual gene relative to the altered gene expression changes after exposure under original HDOM or the residual HDOM after adsorption by iron oxyhydroxides compared with untreated control. The X axis listed stress response categories and all selected genes (see Table S1 of the Supporting Information). The numbers from 1 to 4 in Y axis represent origin HDOM and residual HDOM components after adsorption by hematite, goethite, and ferrihydrite, respectively. The concentrations of all sample were 10 mg-C/L. TELI values for different stress functional categories including (b) total stress, (c) oxidative stress, (d) protein stress, (e) membrane stress, (f) general stress and (g) DNA stress. Different letters on columns displayed a significant difference based on the least significant difference (LSD) ($P < 0.05$).

Fig. 6. Proposed schematic for the genotoxicity evolution of HDOM induced by molecular fractionation at soil-water interface. H, G, and F represent hematite, goethite, and ferrihydrite, respectively.

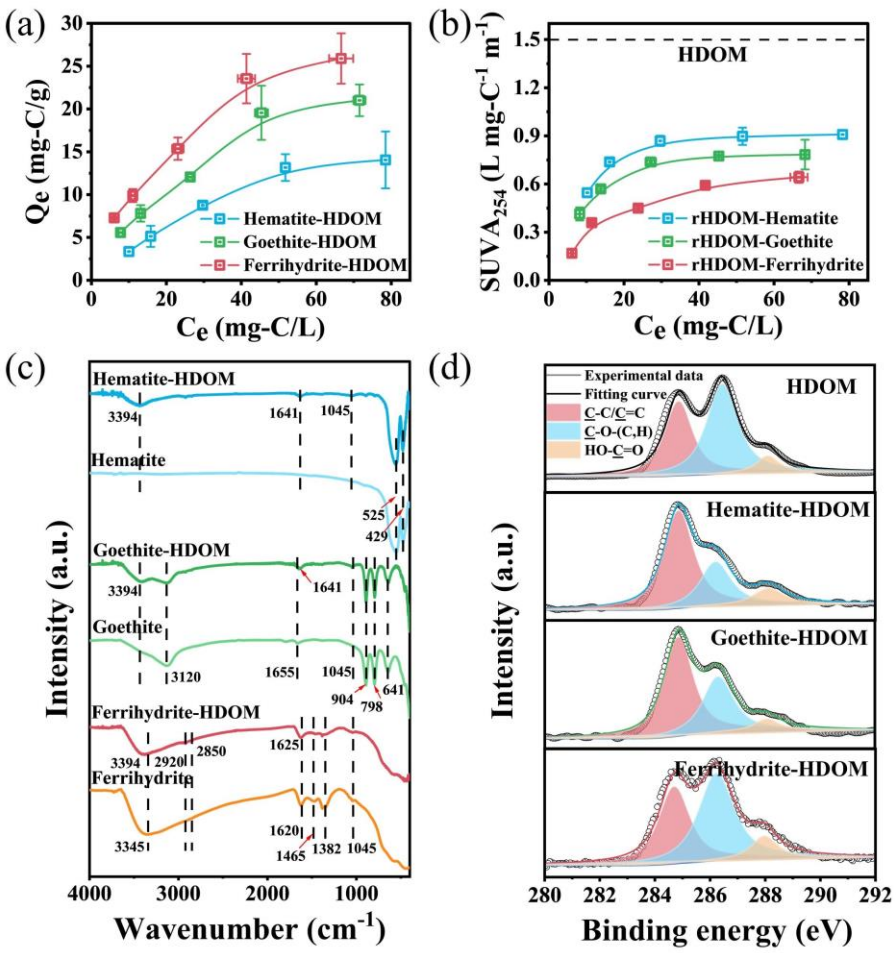


Fig. 1. (a) Adsorption isotherms of HDOM on hematite, goethite, and ferrihydrite (pH 6.5, 10 mM $NaNO_3$). (b) $SUVA_{254}$ of HDOM before and after sorption on hematite, goethite, and ferrihydrite. (c) FTIR spectra of three iron oxyhydroxides before and after HDOM sorption. (d) High-resolution of C1s spectrums with curve-fitting for original HDOM and iron oxyhydroxides-adsorbed HDOM components. Hematite/Goethite/Ferrihydrite-HDOM denote HDOM components adsorbed by hematite, goethite, and ferrihydrite, respectively. rHDOM- Hematite/Goethite/Ferrihydrite denote residual HDOM components after adsorption by hematite, goethite, and ferrihydrite, respectively.

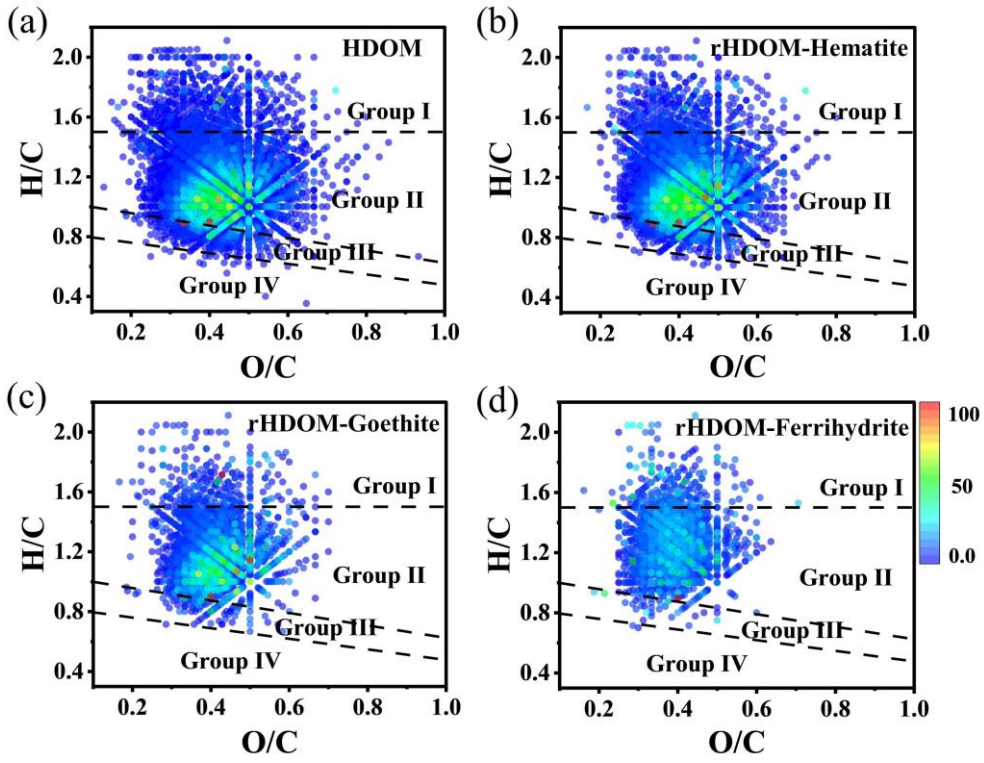


Fig. 2. van Krevelen (VK) diagrams revealed molecular composition of HDOM (a) before and after adsorption on (b) hematite, (c) goethite, (d) ferrihydrite, respectively. Four categories are divided by the aromaticity index (AI) and H/C cutoffs as follow: aliphatic compounds (Group I, $1.5 \leqslant H/C \leqslant 2.0$), highly unsaturated and phenolic compounds (Group II, $H/C < 1.5$ and $AI \leqslant 0.50$), vascular plant-derived polyphenols (Group III, $0.50 \leqslant AI \leqslant 0.66$), and combustion-derived condensed polycyclic aromatics (Group IV, $AI > 0.66$). Color bar represents the relative abundance of molecules with % unit.

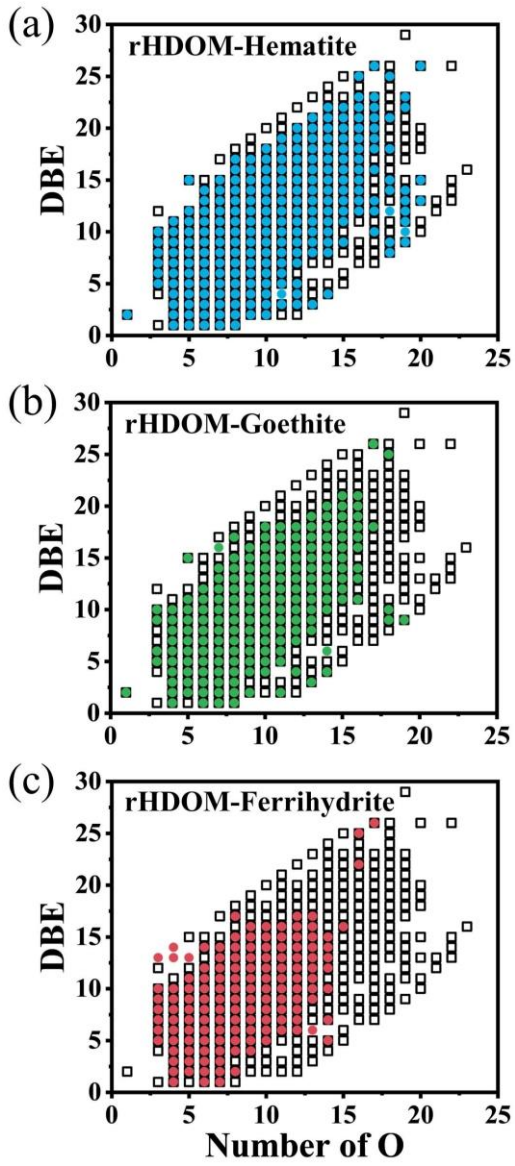


Fig. 3. Plots of Double-bond equivalence (DBE) versus the number of O atoms in molecular formulas of HDOM after adsorption on (a) hematite, (b) goethite, and (c) ferrihydrite, respectively. The black hollow square represents the original HDOM molecules, and the blue, green, and red hollow circles represent the residual HDOM molecules after sorption by hematite, goethite, and ferrihydrite, respectively.

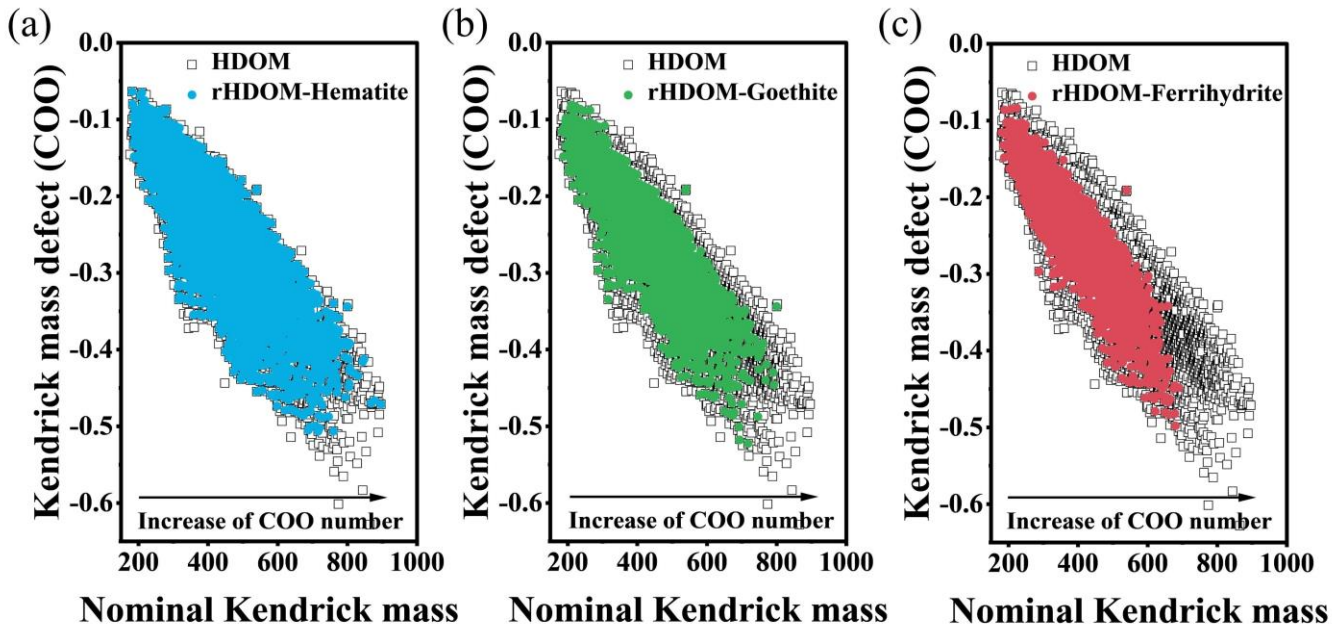


Fig. 4. Kendrick mass analysis of CHO molecules after sorption by (a) hematite, (b) goethite, and (c) ferrihydrite. Formulas that share the same KMD (COO) value are carboxylation homologs. The black hollow square represents the original HDOM molecules and the blue, green, and red hollow circles represent the residual HDOM molecules after sorption by hematite, goethite, and ferrihydrite, respectively.

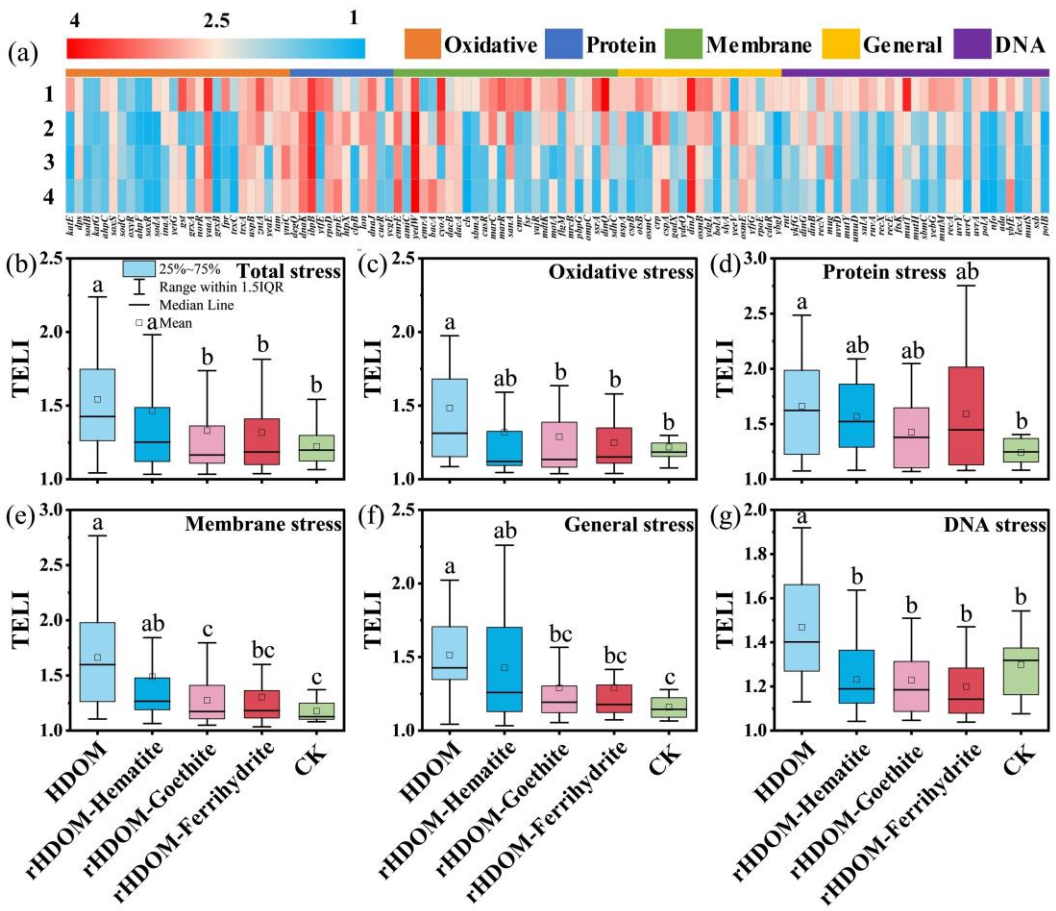


Fig. 5. Genotoxicity evolution of HDOM before and after sorption by three iron oxyhydroxides. (a) Heatmap of TELI value for each individual gene relative to the altered gene expression changes after exposure under original HDOM or the residual HDOM after adsorption by iron oxyhydroxides compared with untreated control. The X axis listed stress response categories and all selected genes (see Table S1 of the Supporting Information). The numbers from 1 to 4 in Y axis represent origin HDOM and residual HDOM components after adsorption by hematite, goethite, and ferrihydrite, respectively. The concentrations of all sample were 10 mg-C/L. TELI values for different stress functional categories including (b) total stress, (c) oxidative stress, (d) protein stress, (e) membrane stress, (f) general stress and (g) DNA stress. Different letters on columns displayed a significant difference based on the least significant difference (LSD) ($P < 0.05$).

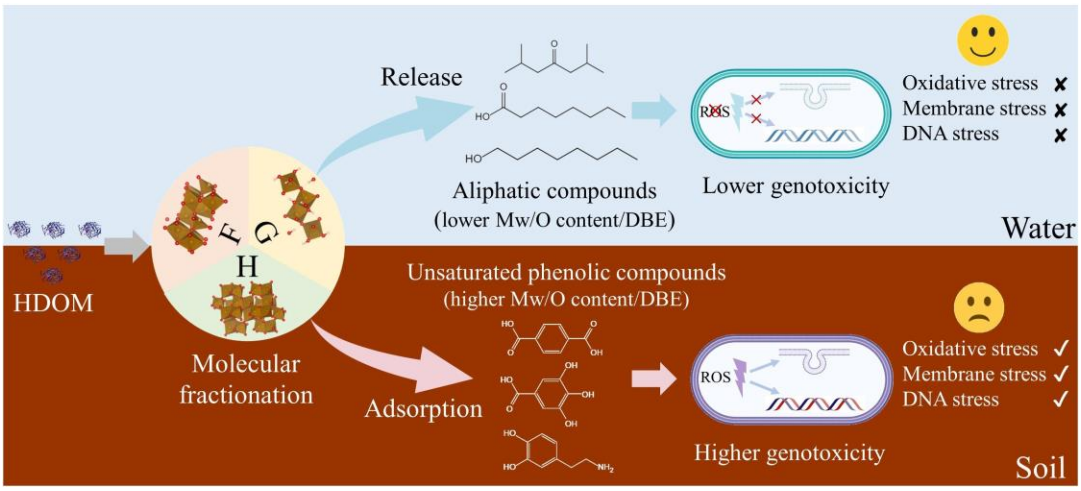


Fig. 6. Proposed schematic for the genotoxicity evolution of HDOM induced by molecular fractionation at soil-water interface. H, G, and F represent hematite, goethite, and ferrihydrite, respectively.